



HAL
open science

The Solar Probe Plus Radio Frequency Spectrometer: Measurement requirements, analog design, and digital signal processing

M. Pulupa, S. D Bale, J. Bonnell, T. Bowen, N. Carruth, K. Goetz, D.
Gordon, P. Harvey, M. Maksimovic, J. Martínez-oliveros, et al.

► To cite this version:

M. Pulupa, S. D Bale, J. Bonnell, T. Bowen, N. Carruth, et al.. The Solar Probe Plus Radio Frequency Spectrometer: Measurement requirements, analog design, and digital signal processing. *Journal of Geophysical Research Space Physics*, 2017, 122 (3), pp.2836-2854. 10.1002/2016JA023345 . hal-02265982

HAL Id: hal-02265982

<https://hal.science/hal-02265982>

Submitted on 1 Jan 2022

HAL is a multi-disciplinary open access archive for the deposit and dissemination of scientific research documents, whether they are published or not. The documents may come from teaching and research institutions in France or abroad, or from public or private research centers.

L'archive ouverte pluridisciplinaire **HAL**, est destinée au dépôt et à la diffusion de documents scientifiques de niveau recherche, publiés ou non, émanant des établissements d'enseignement et de recherche français ou étrangers, des laboratoires publics ou privés.

Copyright

TECHNICAL
REPORTS:
METHODS

10.1002/2016JA023345

Special Section:

Measurement Techniques in
Solar and Space Physics: Fields

Key Points:

- The RFS is a newly designed receiver and spectrometer for Solar Probe Plus
- The RFS provides the FIELDS suite with high-frequency measurements of radio bursts and quasi-thermal noise
- The RFS is optimized for flexible operations and minimal use of resources

Supporting Information:

- Supporting Information S1
- Table S1
- Table S2
- Table S3
- Table S4

Correspondence to:

M. Pulupa,
pulupa@ssl.berkeley.edu

Citation:

Pulupa, M., et al. (2017), The Solar Probe Plus Radio Frequency Spectrometer: Measurement requirements, analog design, and digital signal processing, *J. Geophys. Res. Space Physics*, 122, 2836–2854, doi:10.1002/2016JA023345.








Received 15 AUG 2016

Accepted 22 FEB 2017

Accepted article online 3 MAR 2017

Published online 30 MAR 2017

The Solar Probe Plus Radio Frequency Spectrometer:
Measurement requirements, analog design,
and digital signal processing

M. Pulupa¹ , S. D. Bale^{1,2}, J. W. Bonnell¹ , T. A. Bowen^{1,2}, N. Carruth^{1,2}, K. Goetz³ , D. Gordon¹, P. R. Harvey¹ , M. Maksimovic⁴, J. C. Martínez-Oliveros¹ , M. Moncuquet⁴ , P. Saint-Hilaire¹, D. Seitz¹, and D. Sundkvist¹ 

¹Space Sciences Laboratory, University of California, Berkeley, California, USA, ²Physics Department, University of California, Berkeley, California, USA, ³School of Physics and Astronomy, University of Minnesota, Minneapolis, Minnesota, USA, ⁴LESIA, Observatoire de Paris, Meudon, France

Abstract The Radio Frequency Spectrometer (RFS) is a two-channel digital receiver and spectrometer, which will make remote sensing observations of radio waves and in situ measurements of electrostatic and electromagnetic fluctuations in the solar wind. A part of the FIELDS suite for Solar Probe Plus (SPP), the RFS is optimized for measurements in the inner heliosphere, where solar radio bursts are more intense and the plasma frequency is higher compared to previous measurements at distances of 1 AU or greater. The inputs to the RFS receiver are the four electric antennas mounted near the front of the SPP spacecraft and a single axis of the SPP search coil magnetometer (SCM). Each RFS channel selects a monopole or dipole antenna input, or the SCM input, via multiplexers. The primary data products from the RFS are autospectra and cross spectra from the selected inputs. The spectra are calculated using a polyphase filter bank, which enables the measurement of low amplitude signals of interest in the presence of high-amplitude narrowband noise generated by spacecraft systems. We discuss the science signals of interest driving the RFS measurement objectives, describe the RFS analog design and digital signal processing, and show examples of current performance.

Plain Language Summary Solar Probe Plus (SPP) is a NASA mission which will travel much closer to the Sun than any previous spacecraft. The FIELDS experiment on SPP is composed of sensors (antennas and magnetometers) and receivers which will measure the electric and magnetic fields in this unexplored region. This paper describes the Radio Frequency Spectrometer (RFS), a receiver which will measure radio waves up to 19.2 MHz. We describe the types of radio signal sources present in interplanetary space close to the Sun, show how the design of the RFS makes it possible to measure these sources, and demonstrate the current performance of the receiver.

1. Introduction

The NASA Solar Probe Plus (SPP) spacecraft [Fox *et al.*, 2015] will launch in 2018 on a mission to study the structure of the lower corona, the physics of heating and acceleration of the solar wind, and the acceleration of energetic particles close to the Sun. The SPP spacecraft will orbit the Sun in a highly elliptical trajectory, using Venus gravity assists to gradually lower its perihelion from an initial value of 35.7 R_{\odot} to a closest approach distance of 9.86 R_{\odot} from the center of the Sun. The part of each orbit below 0.25 AU (53.7 R_{\odot}) is known as the “encounter phase.” During the encounter phase, which lasts approximately 12 days, the SPP instruments will make measurements of electric and magnetic fields, plasma ions and electrons, energetic particles, and white light images. The unique orbit of SPP will enable measurements of newly accelerated coronal plasma, undisturbed by transport effects which alter the properties of the solar wind as it travels from its birthplace in the corona to the greater distances explored by previous spacecraft.

The measurements of electric and magnetic fields for SPP will be made by the FIELDS instrument suite [Bale *et al.*, 2016], which is equipped to measure electric fields from DC to 19.2 MHz and magnetic fields from DC up to 1 MHz. Figure 1 shows the configuration of the FIELDS sensors on the SPP spacecraft. The spacecraft coordinate system and the coordinate system of the search coil magnetometer (SCM) are indicated in blue and red, respectively.

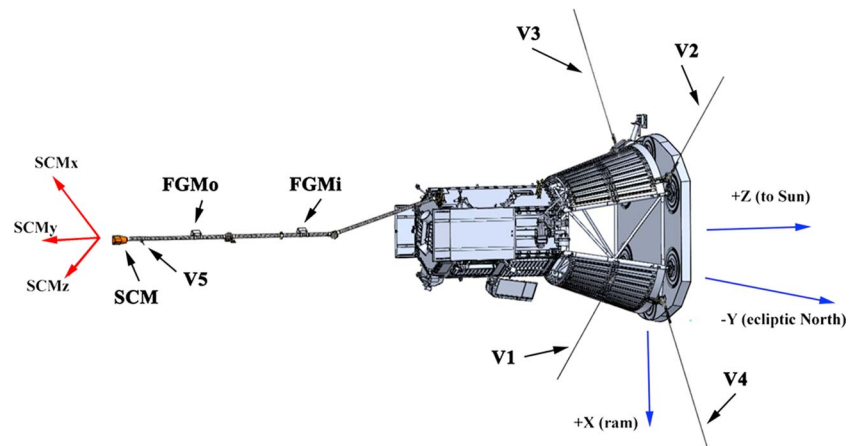


Figure 1. FIELDS sensor locations on the SPP spacecraft. The RFS input comes from the V1–V4 antennas and the MF winding of the SCM. The V5 and fluxgate magnetometer sensors on the magnetometer boom are not used as inputs to the RFS. Figure from *Malaspina et al.* [2016].

FIELDS measures electric fields with four 2 m antennas (V1–V4) mounted near the SPP heat shield in the spacecraft X–Y plane, and one sensor (V5) mounted on the boom at the back of the spacecraft. Preamplifiers mounted near the base of the V1–V4 antennas amplify the signals measured at the antenna terminals, and provide low-frequency (LF), medium-frequency (MF), and high-frequency (HF) outputs. The V5 sensor is a simple voltage probe consisting of two short elements (tip to tip length ~21 cm), which will be used to measure LF and MF electric fields and plasma waves, determine the electrostatic center of the spacecraft, and characterize the effects of the spacecraft plasma wake. The V5 preamplifier does not feature an HF output.

Magnetic fields are measured with two fluxgate magnetometers (MAGs), as well as a search coil magnetometer (SCM), all mounted on the same boom at the antisunward side of the spacecraft. The two MAGs and the SCM each measure three axes simultaneously, with the MAGs most sensitive at lower frequencies and the SCM more sensitive at higher frequencies. Each axis of the SCM has a low-frequency (LF) winding sensitive to fluctuations in the range from 10 Hz to 50 kHz. The SCM X axis also has an additional medium-frequency (MF) winding, sensitive to fluctuations from 1 kHz to 1 MHz. The SCM X axis is parallel to the spacecraft X–Z plane and is oriented 45° from the spacecraft X–Y plane.

The RFS (Radio Frequency Spectrometer) is the highest-frequency component of the SPP FIELDS suite, with a bandwidth of 10 kHz to 19.2 MHz. The RFS is a two-channel digital spectrometer, which uses as its inputs the HF output from the V1–V4 antenna preamplifiers and the MF winding of the SCM. The input to each simultaneously measured channel of the RFS is controlled by multiplexers, so each channel can take as input either a single electric antenna (monopole mode), the analog difference between two antennas (dipole mode), or the input from the SCM. A block diagram showing the inputs to the RFS is shown in Figure 2.

Previous missions carried solar and planetary radio experiments with similar scientific goals and requirements as the RFS. These experiments, such as the Ulysses/URAP RAR/PFR receivers, the Wind/WAVES TNR/RAD1-2 receivers, the Cassini/RPWS investigation, and the STEREO/WAVES LFR/HFR receivers [Stone et al., 1992; Bougeret et al., 1995; Gurnett et al., 2004; Bougeret et al., 2008], like the RFS, were designed to observe remote radio emissions and fluctuations close to the electron plasma frequency. These radio receivers used a superheterodyne technique, mixing the measured signal with a local oscillator to produce a low-cadence envelope signal. SPP/FIELDS had originally planned for such a receiver; however, for programmatic reasons this proved to be impossible. The RFS was instead designed and built to make these critical measurements. RFS is a passband receiver and a new design.

The RFS bandwidth covers the plasma frequency f_p , which will range from ~100 to ~750 kHz during the encounter phase [Bale et al., 2016]. Below the plasma frequency ($f \ll f_p$), remotely generated transverse electromagnetic (TEM) radio waves do not propagate through the plasma and the measurements made by the sensors are due to in situ plasma waves and turbulent fluctuations. For frequencies significantly above the plasma frequency ($f \gg f_p$), plasma effects are unimportant and the medium behaves like a vacuum in which electromagnetic waves can freely propagate. Radiofrequency sources such as solar radio bursts and

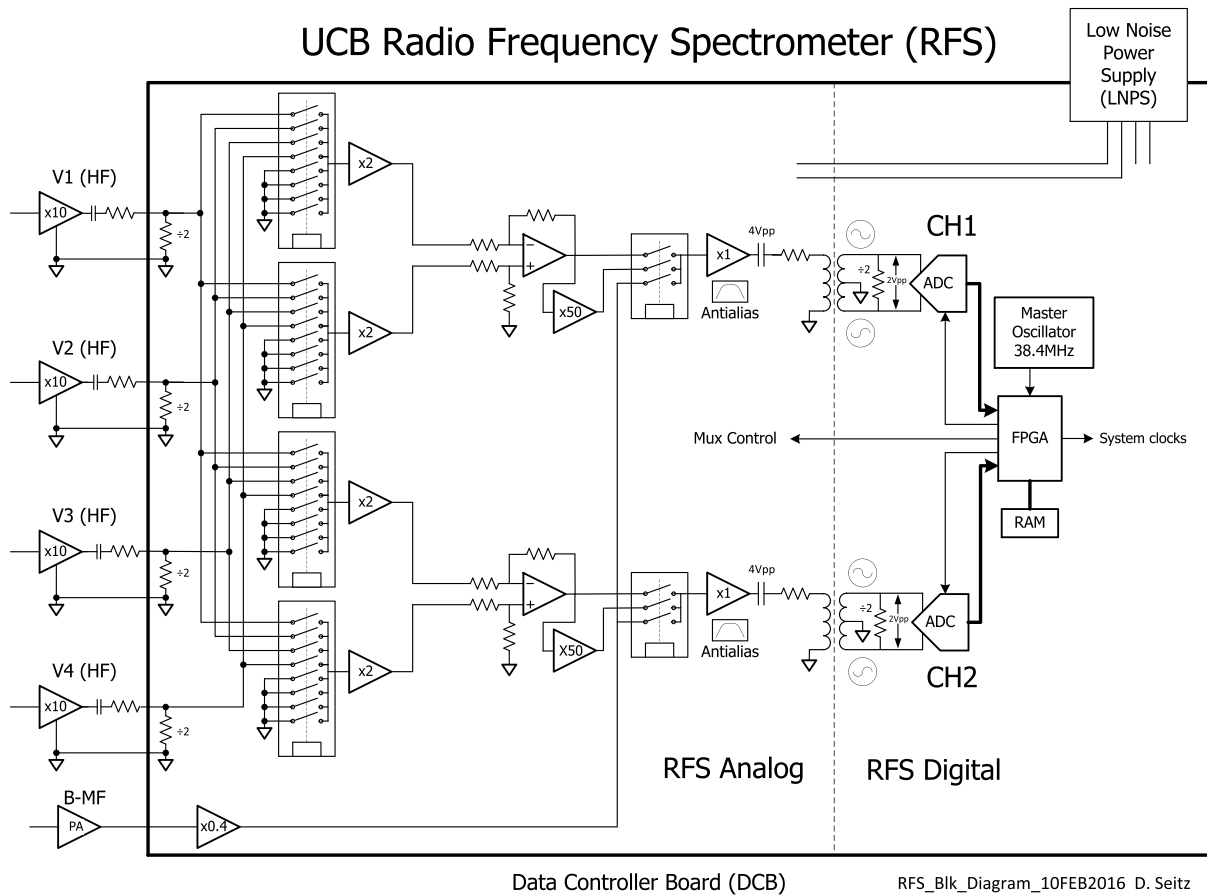


Figure 2. RFS block diagram. Inputs to the RFS are shown at the left. The RFS analog and digital sections are physically located on the DCB.

the galactic synchrotron spectrum predominate at these frequencies. Near the plasma frequency ($f \sim f_p$), resonance of electrostatic waves (corresponding to a zero of the plasma dielectric function) creates a peak in the measured spectrum, with the location and shape of the peak determined by the local electron parameters [Meyer-Vernet and Perche, 1989]. Analysis of the resulting spectrum, via a technique known as quasi-thermal noise (QTN) spectroscopy, can provide accurate absolute plasma electron density and temperature measurements [Issautier et al., 2001; Salem et al., 2001]. Effective QTN analysis depends on sufficient spectral resolution, antennas which are long compared to the Debye length of the plasma, and a highly sensitive receiver. For the RFS receiver, optimal conditions for measuring both electron density and temperature occur near perihelion, while conditions at the start of the encounter phase near 0.25 AU will be less favorable. The capability of RFS to measure QTN is discussed further in section 2.3.

2. Signal and Noise Sources

The digital and analog design process for the RFS required accurate estimates of the amplitudes of the various signal and noise sources. In the literature and the technical design requirements, signal levels are typically presented as spectra in calibrated physical units such as sfu, $W/m^2/Hz$, or V^2/Hz . For purposes of receiver design, it is necessary to translate these values into RMS or peak to peak voltages at the antenna terminals which will be amplified by the preamplifier, passed through the RFS analog section, and digitized by the RFS analog to digital converters (ADCs).

For a source which consists of TEM radio waves (such as the galactic background or remote observations of radio bursts), the conversion of units of flux (S , in units of $W/m^2/Hz$) to measured power (P , in units of V^2/Hz) is given by [e.g., Eastwood et al., 2009]

$$P [V^2/Hz] = S [W/m^2/Hz] \times Z_0 L_{eff}^2 \Gamma^2 \tag{1}$$

where Z_0 is the impedance of free space ($Z_0 \approx 377 \Omega$), L_{eff} is the antenna effective length, and Γ is the capacitive gain factor. Scale model rheometry offers a means of characterizing antenna effective length [Rucker et al., 1996; Bale et al., 2008; Oswald et al., 2009] by measuring the potential differences induced on a scale model of a spacecraft immersed in an electrolytic tank in which a known, well-calibrated electric field is maintained. Rheometry measurements using a scale model of the SPP spacecraft were performed at UC Berkeley in 2015. The rheometry experiment estimated the effective electrical length of opposing FIELDs dipoles at $L_{\text{eff,dipole}} = 2.67 \text{ m} \pm 10\%$. In the same experiment, the monopole effective length was estimated at $L_{\text{eff,monopole}} = 1.51 \text{ m} \pm 10\%$. The uncertainty in the effective monopole and dipole lengths represents both inherent uncertainty in the estimates as well as variation between individual monopoles and dipoles due to asymmetries in the spacecraft chassis.

At the high frequencies relevant to RFS measurements ($f \gg f_{\text{ce}}, f_p$), the gain factor Γ arises from voltage division between the coupling of the whip of the antenna to external potential fluctuations (the vacuum antenna capacitance, C_a) and the stray capacitance C_s :

$$\Gamma = C_a / (C_a + C_s) \quad (2)$$

The antenna capacitance can be estimated from the antenna length L and radius a as

$$C_A = \frac{2\pi \epsilon_0 L}{\ln(L/a) - 1} \quad (3)$$

yielding 18 pF for a 2 m antenna with a 1.5 mm radius.

The stray capacitance is the sum of the capacitance provided by the coupling of the antenna to nearby conductive structures on and in the antenna itself and on the spacecraft (the “base” capacitance), the capacitance of the cables connecting the antenna to the preamplifier, and the input capacitance of the preamplifier electronics.

The cable and preamplifier input capacitances were both measured in bench testing. The base capacitance is difficult to estimate analytically or numerically but can be measured using a physical model of the antenna and a capacitance meter. Such a characterization was performed at UC Berkeley in 2013 using a full-scale model of the antenna, following a procedure similar to that used for the STEREO/SWAVES antennas [Bale et al., 2008]. The total measured stray capacitance was 26 pF, yielding a Γ of 0.40.

Using these values for Γ and L_{eff} , values for P can be calculated from estimates of S . From the calculated value of P and the measured gain of the preamplifier and RFS analog electronics, the amplitude of the digitally sampled waveforms can be calculated in onboard engineering units (counts in the RFS ADCs).

For Type III radio burst and QTN sources, we estimated the intensity at several radial distances in the SPP orbit, as shown in Figure 3. These distances of 54, 35, and 10 R_s correspond to the start of the encounter phase at 0.25 AU, the first perihelion after launch in 2018, and the closest approach, respectively. An overview of expected signal sources, as well as a measurement of system noise, is shown in Figure 3. (The measured noise will be described in more detail in section 6. The noise data is the same data plotted in Figure 9, multiplied by a factor of $\sqrt{2}$. This multiplication is used because Figure 3 shows amplitudes for a dipole configuration, while Figure 9 shows monopole data, and the noise from two monopole channels adds in quadrature when making a dipole measurement.) The sources shown in the figure are discussed in the sections below.

2.1. Radio Bursts

Type III solar radio bursts [Dulk, 1985, 2000; Gopalswamy, 2004; Reid and Ratcliffe, 2014] are generated by beams of electrons accelerated into interplanetary space by solar flares. Velocity dispersion of the beam along interplanetary magnetic field (IMF) lines creates unstable bump on tail electron velocity distribution functions (eVDFs). The instability in the eVDF is relaxed by growth of Langmuir waves, which are electrostatic fluctuations occurring at the local plasma frequency f_p . The Langmuir waves in turn can mode convert to radio emission at f_p or its harmonics. As the accelerated electrons continue to travel outward from the Sun along the IMF lines, the plasma frequency decreases, and the frequency of Type III emission decreases correspondingly. Analysis of the frequency-drifting signal offers considerable information on the properties of the accelerated electron beam and the structure of the IMF [Reiner and MacDowall, 2015, and references therein].

Krupar et al. [2014] analyzed 152 Type III radio bursts observed with the STEREO/WAVES receivers between the frequencies of 125 kHz and 16 MHz over a period of several years. From this data set, they determined the

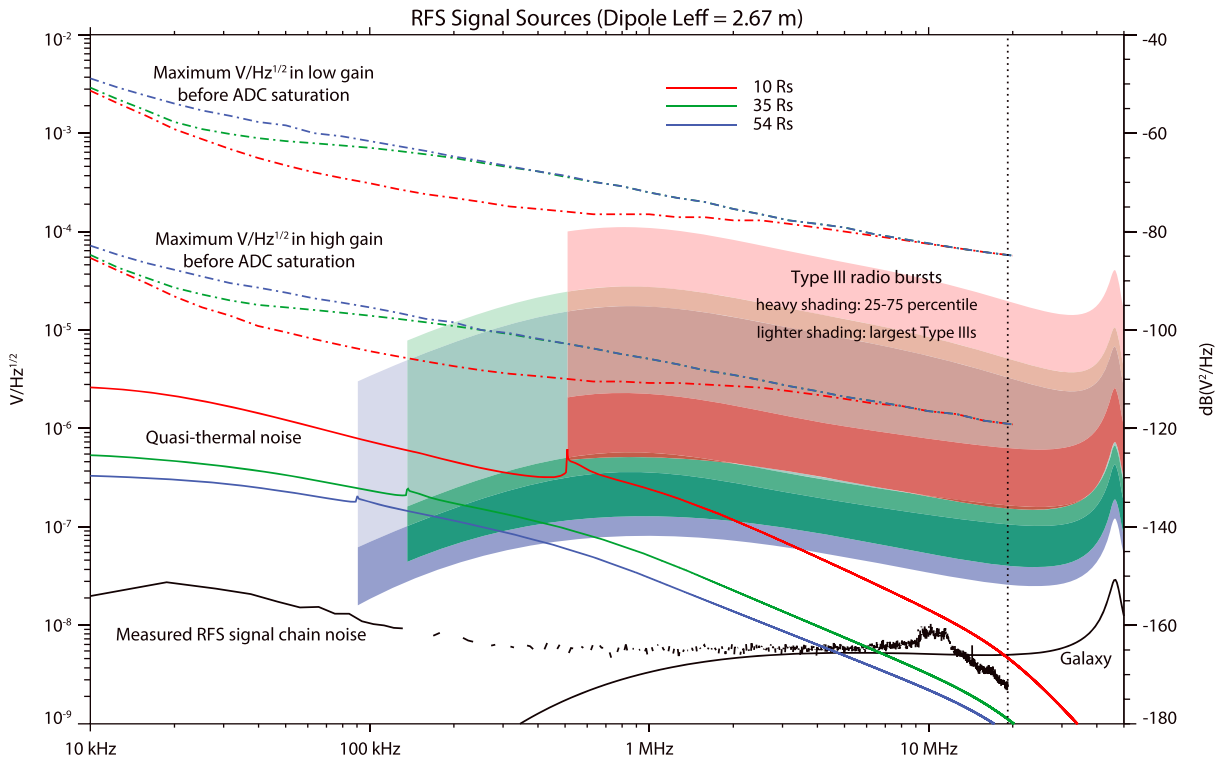


Figure 3. RFS signal and noise sources. The vertical axis is in units of spectral density, referred to the input of the FIELDS HF preamplifiers.

statistical distribution of Type III flux density S_v as a function of frequency at ~ 1 AU. The flux density distribution reached a maximum near 1 MHz (corresponding to a heliocentric distance of ≈ 8 solar radii for fundamental emission, and ≈ 14 for harmonic emission), with the 25th to 75th percentile values of S_v ranging from $\sim 8 \times 10^{-19}$ to 1.5×10^{-17} W/m²/Hz.

These curves of estimated Type III intensity, scaled to several solar radial distances, are shown in Figure 3 as blue- ($54 R_s$), green- ($35 R_s$), and red- ($10 R_s$) shaded ribbons. The flux density S_v scales approximately with the square of the radial distance from the Sun, with corrections due to source location (the radiation originates at some distance from the Sun) and nonzero source size. To estimate the heliocentric distance of the emission region, we have used the radial density profile of *Leblanc et al.* [1998], and for estimates of source size we have used Type III observations found in *Steinberg et al.* [1985].

The most intense Type III radio bursts occur with peak S_v up to 10^{-14} W/m²/Hz at 1 MHz at observed distances of ~ 1 AU [Weber, 1978]. These large Type IIIs are indicated in Figure 3 by lightly shaded extensions of the blue, green, and red ribbons.

To estimate the occurrence rate of intense Type IIIs, we modeled the 1 AU, 1 MHz distribution of Type III bursts given in *Krupar et al.* [2014] as a lognormal probability distribution function (PDF) of occurrence rate. Combined with the total time interval of the Type III study, this yields an occurrence rate for Type IIIs at a given flux density (i.e., the PDF has units of number of bursts/s/log S_v).

The PDF of Type III occurrence rate can then be scaled from 1 AU to the different radial distances encountered by SPP. Combining the scaled profiles with a time profile of radial distance for the entire mission, a total number of expected bursts at a given flux density for the mission can be obtained (units number of bursts/mission/log S_v). This approach generates an estimated ~ 20 Type III bursts during the SPP mission with $S_v > 10^{-14}$ W/m²/Hz (as observed at the spacecraft). The estimated probability of a radio burst large enough to saturate the instrument in low-gain mode (see section 3.4) can also be calculated from the occurrence rate PDF and is estimated at $\sim 0.1\%$ during the duration of the mission.

We note that the estimates described above have large uncertainties, since they are based on 1 AU observations. Scattering and ducting effects as well as inhomogeneity in the solar wind plasma can affect radio

emission as it travels from the source region, which can introduce errors into the calculation of S_ν in the inner heliosphere based on observed S_ν at 1 AU.

Section 3.4 describes the different gain stages of the RFS, which enable measurement of both the large Type IIIs and the smaller amplitude signals described below.

Type II interplanetary radio bursts, which are generated by shock-accelerated electrons upstream of coronal mass ejections (CMEs), occur in the same frequency range as Type III bursts and are of comparable scientific interest for SPP. However, the amplitude of the Type II emission is lower than that of Type IIIs, so the Type IIIs are the driver for determining the high end of the RFS dynamic range.

2.2. Galactic Synchrotron Spectrum

In order to accurately calibrate the RFS, it is helpful to use the galactic background radio spectrum [Novaco and Brown, 1978; Cane, 1979; Hillan et al., 2010] as a source of known intensity that has been measured accurately by several previous missions. The galactic spectrum is constant in time and nearly isotropic in angular distribution [Manning and Dulk, 2001], with a broad peak near 1 MHz, which lies within the RFS bandwidth. The galactic signal can therefore be used together with measured antenna parameters such as the effective length and base capacitance to derive an accurate absolute calibration [Zaslavsky et al., 2011].

Observing the galactic noise is a significant challenge for RFS, due to the short length of the SPP/FIELDS electric antennas. For FIELDS, the length of the antenna is 2 m for a monopole, compared to a length of 6 m for the S/WAVES antennas and tens of meters for spin-stabilized spacecraft such as Wind and Ulysses. Unlike other science signals of interest, the galactic noise amplitude does not increase with decreasing solar distance. For an effective length of 2.67 m, the galactic synchrotron signal is of the same order of magnitude as the input noise to the FIELDS preamplifier. Therefore, to clearly observe the signal, the preamplifier and receiver must be carefully designed and calibrated, so the noise can be accurately subtracted from the signal.

2.3. Quasi-Thermal Noise

The quasi-thermal noise (QTN) spectrum is generated by the motion of plasma electrons and ions in the vicinity of the spacecraft. The spectrum, measured in V^2/Hz , depends on the antenna impedance and gain, which in turn depend on both the antenna geometry and the parameters of the local plasma [Couturier et al., 1981; Meyer-Vernet and Perche, 1989]. The peak in the QTN spectrum at the plasma frequency f_p is determined by the total electron density n_e , from the expression $f_p = 8980 \sqrt{n_e}$, with f_p in Hz and n_e in cm^{-3} . The location of the plasma peak is unaffected by the spacecraft potential, making it a useful absolute calibration for the SWEAP electron plasma instruments on board SPP [Kasper et al., 2015].

The plasma peak is easily measurable when the physical lengths of the antennas are much longer than the local Debye length ($L \gg L_D$). When this condition does not hold, the amplitude and width of the plasma peak can be too small for the peak to be resolved. In this case, other sources such as shot noise can dominate the observations [Zouganelis et al., 2010, 2010], although it is still possible to extract some information from the spectrum [Martinović et al., 2016].

When the plasma peak is discernible in the spectrum, the electron density can be immediately determined from the plasma frequency. Just below the plasma peak, the spectrum exhibits a flat region, known as the thermal plateau, with an amplitude determined by the thermal electron temperature [Meyer-Vernet and Perche, 1989]. When the plasma peak is prominent enough that the plateau is distinguishable from the background, the electron temperature can be calculated from the plateau amplitude without a full fit to the QTN spectrum [Moncuquet et al., 2005].

The plasma peak will be most prominent and the electron plasma parameters most amenable to analysis, near closest approach. With a very prominent and well-resolved peak, it is possible to fit not only the electron density and core temperature but also the suprathermal electron density, temperature, and power law index (κ), as well as the ion bulk flow speed. Closest approach is also the part of the orbit where the effects of spacecraft charging will be strongest [Ergun et al., 2010; Guillemant et al., 2012], so the ability of the QTN spectrum to provide electron parameters will be most helpful for the plasma instrumentation.

The Debye length during the SPP encounter phase is expected to vary from ~ 1.68 m at $54 R_s$ to ~ 84 cm at $\sim 10 R_s$ [Bale et al., 2016]. Several example QTN curves, for distances of 54, 35, and $10 R_s$, are plotted in Figure 3. At the start of the encounter phase, the plasma peak is expected to be only a small bump on the spectrum, which may be barely discernible from the noise generated by fluctuations in the plasma.

The peak will grow in amplitude and prominence above the surrounding background as SPP gets closer to the Sun, due to the increase of density and plasma frequency and the corresponding decrease in Debye length. At closest approach, we expect that it will be possible to perform full QTN fits on the spectrum, resulting in a full set of solar wind plasma parameters. At greater distances, full fits may become impractical, but a simpler method can still be used to estimate thermal density and temperature [Moncuquet *et al.*, 2005]. At still greater distances, it may be possible to determine only the total electron density from the plasma peak, and near the outer limits of the encounter phase the peak may disappear entirely if the ratio of L to L_D becomes small enough. The radial thresholds at which various methods are possible will depend on the plasma environment and the on-orbit performance of the instrument.

The RFS signal processing includes an algorithm to analyze and return higher spectral resolution in the vicinity of the plasma peak. This algorithm is discussed in section 5.1.

2.4. Langmuir Waves and Dust

Langmuir waves, discussed above in the context of the creation of remote radio burst emission, are also observed in situ [Kellogg, 2003; Hess *et al.*, 2011]. The amplitude of Langmuir waves for SPP in the inner heliosphere is expected to reach up to ~ 1 V/m near the plasma frequency, orders of magnitude higher than the top end of the RFS dynamic range. When encountering Langmuir waves, the RFS instrument will record saturated waveforms, which will yield compromised, unphysical spectra. Other large-amplitude fluctuations, such as ion acoustic waves, also appear in the solar wind [Briand, 2009] and can have similar effects. In addition to large amplitude waves, dust impacts [Meyer-Vernet *et al.*, 2009; Zaslavsky *et al.*, 2012; Malaspina *et al.*, 2015] are also capable of briefly saturating the RFS receiver, which can distort the spectra, especially in the low-frequency ($f < f_p$) range.

On SPP/FIELDS, these phenomena will be accurately captured by the Time Domain Sampler (TDS) [Bale *et al.*, 2016] and Digital Fields Board (DFB) [Malaspina *et al.*, 2016], which have sufficient dynamic range to make the necessary large-amplitude measurements. In contrast, the high sensitivity RFS receiver is designed to avoid the time periods where these events occur, by keeping track of which waveforms are spoiled by saturation and selecting unaffected intervals for spectral processing. This is possible because the large-amplitude signals typically are of short duration and highly intermittent.

3. Analog Design

The analog design of the RFS is driven by the requirements for high sensitivity, large dynamic range, and use of minimal onboard resources. A high-sensitivity receiver is necessary in order to measure weak signals such as the galactic synchrotron spectrum, while a large dynamic range is required to measure large-amplitude radio bursts without saturating the receiver.

3.1. Accommodation and Board Design

The RFS receiver is physically located on an isolated section of the FIELDS Data Control Board (DCB) [Bale *et al.*, 2016], which is the primary flight computer and spacecraft interface for the FIELDS suite. In order to protect the integrity of RFS signals from possible noise generated on the DCB board, a metal enclosure covers the multiplexers and operational amplifiers of the RFS analog section. The physical boundary visible in the upper right quadrant of Figure 4 contains all of the components to the left of the balun shown on the RFS block diagram in Figure 2. The RFS section of the DCB/RFS is virtually a separate board, with none of the power or ground planes crossing the gap provided at the physical boundary. The placement of components and traces on the board has been optimized to minimize crosstalk and phase delay between the two RFS channels.

The mass of the DCB/RFS board is 439 g, of which approximately 100 g is dedicated to the RFS analog section. The operational power for the DCB/RFS is 2.59 W, of which approximately 0.65 W is used for the RFS analog section. Compared to estimates for the originally proposed stand-alone heterodyne receiver (650 g and 2 W), the RFS uses considerably less mass and power.

3.2. Analog Filtering

Before being digitized, RFS electric and magnetic field inputs are subject to analog passband filtering. For the electric field (V1–V4) measurements, the filter roll on is provided by a single-pole RC high pass filter at the HF input of the preamplifiers, with a -3 dB point at 30 kHz. A three-pole Butterworth low pass filter with a -3 dB point at 16 MHz provides antialiasing immediately prior to the balun.

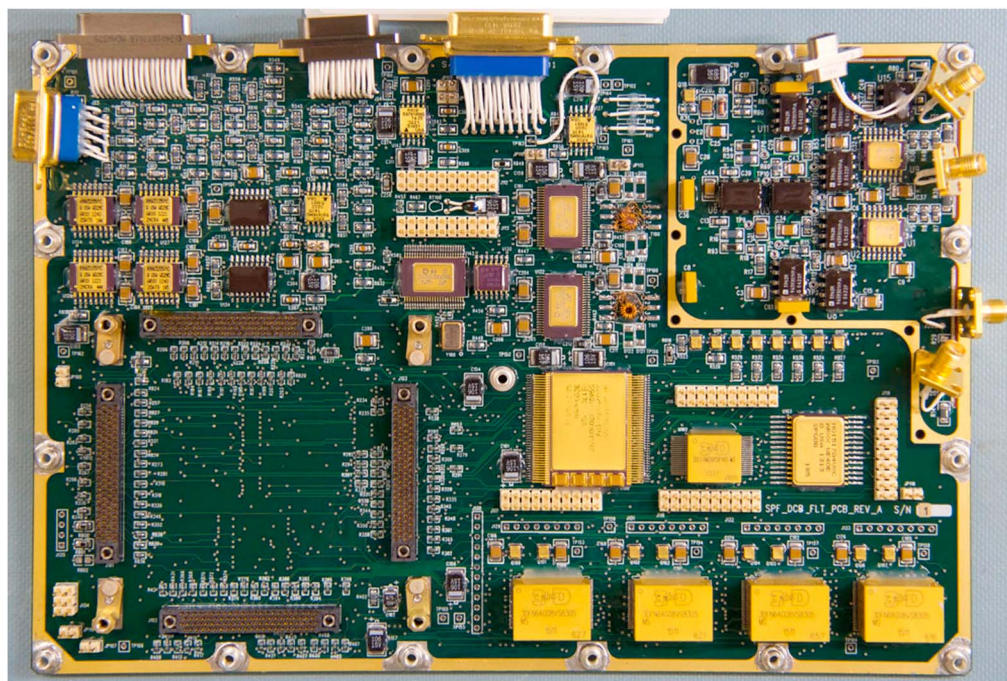


Figure 4. DCB/RFS FM board. The RFS analog electronics are isolated from the main board in the area in the upper right corner of the DCB/RFS. The DCB FPGA is not shown in this image; when installed, the FPGA resides in the space on the lower left side of the board.

For the magnetic field measurements, the analog response is primarily determined by the inherent inductive properties (winding geometry, ferrite core permeability) of the sensor and the electrical properties of its preamplifier. The SCM MF winding is sensitive to signals from 1 kHz to 1 MHz. The RFS analog section also includes a two-pole Butterworth low pass filter for the SCM input, with a -3 dB point at 1 MHz.

3.3. RFS Sensitivity

The sensitivity of the RFS is driven by the desire to observe the galactic synchrotron spectrum, which allows for absolute calibration of the antenna-receiver system. High sensitivity is also critical to measure weak radio bursts, which may be a signature of coronal heating. It has been shown that if weak solar flares contribute significantly to heating the corona, the occurrence distribution of flares (and associated Type III radio bursts) must be sufficiently steep at low energies, with the critical shape of the occurrence distribution specified by Hudson [1991]. Statistics of solar radio bursts have been previously studied using ground-based observatories [Mercier and Trotter, 1997; Saint-Hilaire et al., 2013]. With sensitivity sufficient to observe weak Type IIIs in a different frequency range (<20 MHz), the RFS may either discover an occurrence distribution consistent with heating or, alternatively, place an upper limit on the contribution of small flares to heating of the corona.

In order to observe these small amplitude signals, the input noise of the FIELDS HF preamplifier must be reduced as much as possible. The predicted amplitude for the galactic synchrotron signal measured by RFS is several $\text{nV}/\sqrt{\text{Hz}}$ at the inputs to the preamplifiers. The overall preamplifier input noise, largely driven by the noise of the input JFET, is of the same order of magnitude. The preamplifier components were chosen to optimize tradeoffs maximizing dynamic range, bandwidth, and gain while minimizing power consumption and noise.

3.4. RFS Gain Stages

As shown in the block diagram in Figure 2, a 50X gain can optionally be applied to the RFS V1–V4 inputs prior to analog filtering and digitization of the signal. When this gain is applied, the RFS is in the high-gain mode, and when it is bypassed, the RFS is in low-gain mode. The typical quiet time signals encountered by the RFS, including the QTN spectrum, the synchrotron spectrum, and spacecraft-generated noise, will all be measured by the high-gain stage. High-amplitude signals, such as large Type III bursts in the inner heliosphere, must be measured by the low-gain stage. The operational algorithm for selecting between the high and low-gain stages is described in section 5.1.

The dash-dotted curves in Figure 3 show the maximum spectral density, in $V/\sqrt{\text{Hz}}$, which can be measured by the RFS before the ADCs are saturated. The frequency variation of the curves is driven by the frequency-dependent gain of the preamplifier and RFS analog section. The maximum spectral density also varies as a function of solar distance, as illustrated by the three curves (at 10, 35, and 54 R_s) for both the high and low gain. The variation with distance is due to the changing impedance between the plasma and the antenna (higher density lowers the resistive component of the impedance, increasing the gain at lower frequencies and thereby saturating the ADC at lower input amplitudes).

Signals observed by the SCM in the RFS frequency range are likely to exhibit a smaller dynamic range than the V1–V4 signals (with the exception of strong in situ plasma waves, which will be observed by the TDS and DFB instruments [Bale *et al.*, 2016]). The SCM input to the RFS therefore has a single gain stage, as shown in Figure 2.

4. Digital Signal Processing

The analog outputs from the two RFS channels pass through the primary windings of two baluns, which convert the unbalanced input signals to differential drive output signals with a center tap on the secondary windings. Two ADCs sample the signal at the FIELDS master clock frequency of 38.4 MHz and store the resulting digital waveform in memory on board the DCB. The waveform is then processed into autospectra and cross spectra which are averaged and telemetered to the ground.

The digital filtering and Fourier transform of the sampled data are performed within the DCB FPGA, which is a radiation-hardened Microsemi RTAX4000SL. The two RFS channels are sampled with 12 bit resolution (including one sign bit), and the 12 bit waveform is used as the input to a polyphase filter bank (PFB) algorithm, implemented on the FPGA. The PFB is used to filter spacecraft-generated noise from the science signal of interest. The mathematical details of the PFB algorithm are described in section 4.2. After the PFB, the two channels of filtered waveform data are stored as 16 bit signed integers. These waveforms are then used as inputs to an ($N_{\text{FFT}} = 4096$ points) FFT algorithm, also implemented on the DCB FPGA. The algorithm used is based on standard techniques for performing FFTs of real-valued data [e.g., Press *et al.*, 1992], adapted to optimize performance within the FPGA gate and memory constraints. The output of the FFT is the complex transform of the input waveforms, stored as 24 bit integers. During the FPGA-based stage of the processing, twos complement-signed integer data format is maintained. The performance characteristics of the RFS FPGA-based algorithms were verified by processing waveforms in IDL, C, and ModelSim implementations of the PFB and FFT.

Following the FPGA-based PFB and FFT, flight software processing of RFS spectra includes multiplications (for the calculation of autospectra and cross spectra) and additions (for averaging). As with the FPGA operations, these flight software operations are performed using integer arithmetic, so additional bits are required to store the integer quantities without limiting the available dynamic range. The final uncompressed onboard spectra are stored as 64 bit unsigned (real-valued autospectra) or signed (complex-valued cross spectra) integers. To reduce downlink bandwidth, these integers are compressed in flight software to a 16 bit floating point quantity. The floating point format for autospectra features 6 bits of exponent and 10 bits of mantissa (11 effective bits with an implicit initial mantissa bit), while the format for cross spectra features a sign bit, 6 bits of exponent, and 9 bits of mantissa (10 effective). The floating point compression is not lossless; however, the loss in accuracy due to the compression is small ($<0.1\%$ for the autospectra, and $<0.2\%$ for the cross spectra).

4.1. HFR/LFR

The RFS operational frequency range is 10 kHz–19.2 MHz, where 19.2 MHz is the Nyquist frequency corresponding to the sampling rate of $f_s = 38.4$ MHz. This frequency range is subdivided into the Low-Frequency Receiver (LFR) and High-Frequency Receiver (HFR) ranges, with the primary science of the LFR consisting of the in situ QTN measurement, while the HFR focuses on remote sensing of radio bursts. The LFR sampling cadence is reduced from 38.4 MHz to $f_s = 4.8$ MHz, downsampling by a factor of 8. The downsampling requires the use of an antialiasing CIC filter, described in section 4.3.

For both the LFR and HFR, the raw FFT spectra computed by the DCB contain 2048 frequency bins, at a linear spacing of $\Delta f = f_s/N_{\text{FFT}} = 1171.875$ Hz (LFR) or 9375 Hz (HFR), with a bandwidth of 0–2.4 MHz (LFR) or 0–19.2 MHz (HFR). The raw spectra contain too much data to be telemetered, given the highly limited

downlink bandwidth available for the SPP mission. In its normal mode, the telemetered spectra will consist of 64 selected frequencies covering the range 10 kHz–1.7 MHz (LFR) and 1.3 MHz–19.2 MHz (HFR). At the low end of the LFR range and the high end of the HFR range, the signal will be attenuated by the high and low pass filters from the RFS analog section. The chosen frequencies will be pseudo-logarithmically spaced, allowing for a consistent relative frequency spacing $\Delta f/f$ of $\sim 4.5\%$ throughout their respective frequency ranges.

4.2. The Polyphase Filter Bank

The numerous spacecraft subsystems and instruments on SPP (or any spacecraft) can generate noise emissions, which can be radiated as electromagnetic waves or conducted via the electrical connections between different subsystems. The noise from these spacecraft-generated emissions can exceed the levels of some low-amplitude science signals.

To enable the measurement of these small signals, the spacecraft and instrument teams are required to limit the radiated electric noise of their subsystems as specified in an electromagnetic compatibility (EMC) plan. The SPP EMC plan limits such radiation to specific frequencies given by $150 \text{ kHz} + n \times 50 \text{ kHz}$ ($n = 0, 1, 2, \dots$), with a maximum bandwidth or variability of each peak of $\Delta f/f < 0.02\%$ over the frequency range measured by RFS, and a maximum far-field amplitude which is measured as specified in the MIL-STD-461 RE02 test [United States Department of Defense, MIL, 1999].

The impact of any given peak in the allowed noise spectrum was estimated by converting the maximum far-field E field amplitude to the local potential variation at the antenna location using the known properties of the standard monopole test antenna used in the RE02 test, a dipole radiator model for a given noise source on the spacecraft and worst-case (minimum) source to antenna center distances.

From these parameters, one then could determine what analog and digital signal processing techniques were required to allow the RFS to make radio frequency (RF) science measurements between the noise peaks. This method of making RF measurements in between spacecraft-generated noise peaks is known as the “picket fence” and has been successfully used on previous missions such as STEREO [Bougeret *et al.*, 2008].

In previous missions, the picket fence was implemented along with a superheterodyne receiver, which generated a signal at a given individual frequency and mixed it with the input signal to produce a measurement at that given frequency. The superheterodyne stepped through frequency space, selecting frequencies which were in between the noise-generating frequencies of the picket fence. In contrast, the FFT-based approach of the RFS measures all frequencies in the bandwidth simultaneously, based on the Fourier transforms of the measured waveforms. In order to implement the picket fence algorithm with an FFT approach, the frequency resolution must be sufficiently high and the spectral leakage of the FFT must be minimized.

The FFT frequency resolution (Δf) is determined from the number of samples N_{FFT} and the sampling rate f_s ($\Delta f = f_s/N_{\text{FFT}}$). The sampling rate of the RFS (in the HFR mode) is given by $150 \text{ kHz} \times 2^8 = 38.4 \text{ MHz}$, and the RFS FFT uses 4096 samples. Setting a sampling frequency at a multiple of 150 kHz places the frequency harmonics at regularly spaced intervals in the resulting FFT. With a 4096 point FFT, this value of f_s yields $\Delta f = 9.375 \text{ kHz}$, ensuring that several RFS frequency bins lie in between the narrowband noise lines, which are spaced 50 kHz apart.

The power spectral density (PSD) in the noise lines can be tens of decibels above the PSD for the weakest science signals of interest in the RFS bandwidth. For an FFT using a typical window function, spectral leakage from adjacent noise lines would overwhelm the weaker signal for the frequency bins in between the noise lines [Harris, 1978], rendering the picket fence ineffective. In order to preserve the capability to observe in between the narrowband noise lines, we employ a polyphase filter bank (PFB) [Lyons, 2004; Proakis and Manolakis, 2007; Gary *et al.*, 2010] to reduce the effects of spectral leakage.

The PFB generates an input time series of length N from a longer waveform of length $N \times P = M$ [Chennamangalam, 2011]. The original M point waveform is multiplied by an M point window function. The waveform is split into P sequential segments (known as “taps”) of N samples each (i.e., if the time series is given by x_0, \dots, x_{M-1} , then the first tap is x_0, \dots, x_{N-1} , the second tap is x_N, \dots, x_{2N-1} , and so on). The individual taps are then added together to make a single N sample time series. That time series is then passed to the FFT to generate a spectrum. In effect, each sample in the N sample time series is generated by filtering P samples from the larger time series, using the elements of the window function as filter coefficients.

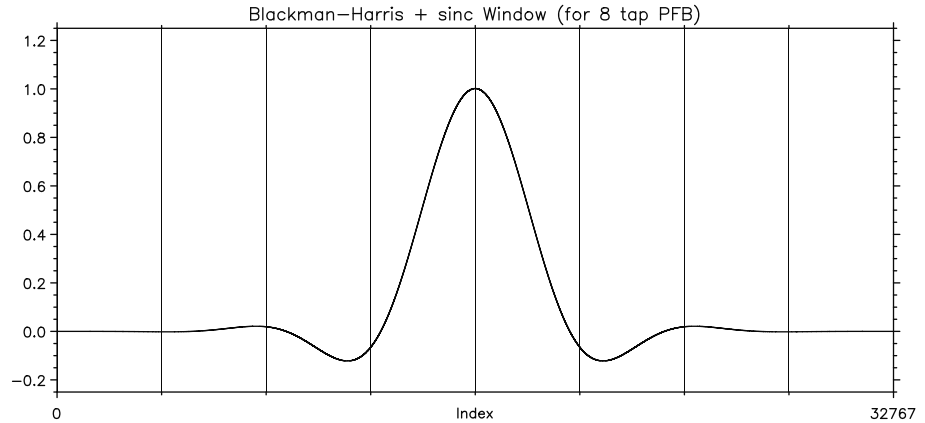


Figure 5. PFB window function. The RFS PFB uses a window function consisting of a Blackman-Harris window multiplied by a sinc function. The vertical lines delineate the boundaries of the eight taps of the RFS PFB algorithm.

The shape of the window function determines the frequency response of the individual frequency bins of the FFT. For example, if a rectangular frequency response is desired, a sinc window would be used, since the Fourier transform of the sinc function is a rectangular function [Chennamangalam, 2011].

The RFS PFB uses a sinc function multiplied by a Blackman-Harris for its window. The Blackman-Harris window is defined as

$$w_0[n] = a_0 - a_1 \cos\left(\frac{2\pi n}{N-1}\right) + a_2 \cos\left(\frac{4\pi n}{N-1}\right) - a_3 \cos\left(\frac{6\pi n}{N-1}\right) \quad (4)$$

where

$$a_0 = 0.35875; \quad a_1 = 0.48829; \quad a_2 = 0.14128; \quad a_3 = 0.01168. \quad (5)$$

The PFB window then consists of the Blackman-Harris window multiplied by a sinc function:

$$w[n] = w_0[n] \times \text{sinc}(\alpha(n - N/2)) \quad (6)$$

where α is a parameter which can be adjusted to narrow or widen the frequency response of the individual PFB bins. The current value of $\alpha = 0.00027$ was chosen to have a flat response near the center of a frequency bin (with a -3 dB point at approximately $\Delta f = \pm 0.5$ bin widths), and with out-of-band rejection of >100 dB for signals with Δf greater than one bin width from the central frequency.

The RFS PFB uses eight taps, so the total length of the input waveform for a single RFS spectrum is $4096 \times 8 = 32,768$. The corresponding window function is shown in Figure 5. Adjusting the values of a_0 , a_1 , a_2 , a_3 , and α allows for fine tuning of the response function.

The response of the RFS PFB (amplitude and phase) is shown in Figure 6. Figure 6a shows the amplitude response, with > -100 dB rejection for out-of-band signals. This response is sufficient to prevent noise from entering the quiet frequency bins in the picket fence where RFS observes science signals. The phase response is shown in Figure 6b, for frequencies where the amplitude response is > -100 dB. The PFB has a minimal effect ($<0.03^\circ$) on the phase of the input signal.

The frequency response of the PFB is determined entirely by the window function, which is stored in onboard tables. A new window function can be generated on the ground, and the PFB tables can be reloaded in-flight, if it is determined during the mission that a narrower or wider response function would be more effective.

4.3. CIC Filtering

RFS can decimate the HFR sample rate by a factor of 8, providing an LFR mode with increased frequency resolution ($\Delta f_{\text{LFR}} = 1171.875$ Hz). Antialiasing for the RFS LFR mode is accomplished with a cascaded integrator comb (CIC) filter. Hogenauer [1981] provides a comprehensive overview of the CIC filter, including a thorough discussion of its merits and implementation. The CIC filter consists of a set of N integrators operating at the

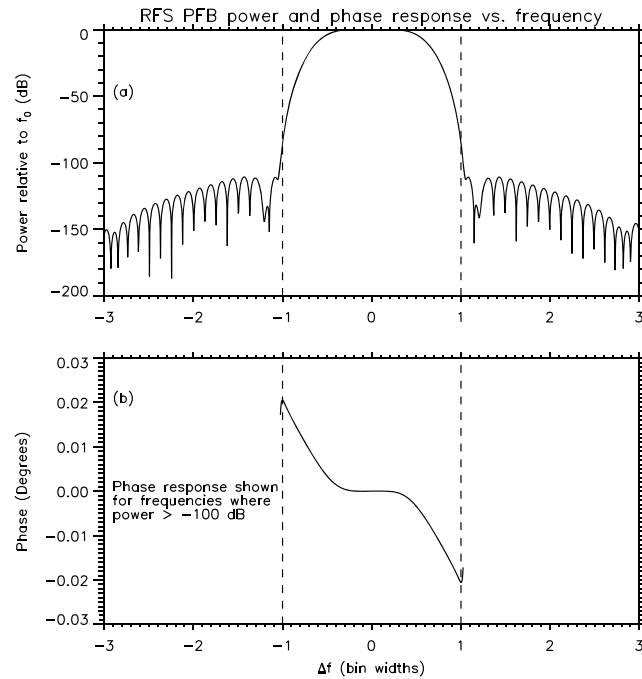


Figure 6. PFB (a) power and (b) phase response for a single-frequency bin of the RFS. Spectral leakage is reduced by >100 dB for signals greater than one bin width from the center of a given frequency bin.

HFR sample rate followed by N comb filters operating at the decimated LFR rate. The integrator stages operate as $y[n] = y[n - 1] + x[n]$ where the output of each integrator is cascaded into the input of the succeeding stage. Each integrator stage has a transfer function given by

$$H_I = \frac{1}{1 - z^{-1}}. \quad (7)$$

The comb stages are described by $y[n] = x[n] - x[n - RM]$ where R is the decimation factor and M is a parameter known as the differential delay. The comb transfer function is given by

$$H_C = 1 - z^{-RM}. \quad (8)$$

Downsampling before the comb cascade increases the CIC filter's efficiency [Donadio, 2000]. After the rate change, the comb operates at a decimated rate described by $y[n] = x[n] - x[n - M]$, effectively decreasing the number of delay elements required in calculating the comb output.

The transfer function of the filter cascade is

$$H_{CIC}(z) = H_I^N(z)H_C^N(z) = \frac{(1 - z^{-RM})^N}{(1 - z^{-1})^N} \quad (9)$$

Evaluating on the complex unit circle $z = e^{i(2\pi f/R)}$ gives the frequency response of the CIC filter as

$$P(f) = \left[\frac{\sin \pi M f}{\sin \frac{\pi f}{R}} \right]^{2N}. \quad (10)$$

Figure 7a shows the gain characteristics of the $N = 4$ stage CIC filter in comparison with a moving average boxcar filter. The CIC filter performs significantly better than a moving average filter as an antialiasing filter. Additionally, the CIC filter provides several economic benefits over FIR filters for implementation in the FIELDS FPGA: no multiplicative steps are required, and storage is reduced by downsampling before passing the integrator stage output to the comb filters.

The RFS uses a four-stage integrator comb filter which can operate with a differential delay set to either one or two. The first null in the $M = 1$ filter occurs at the LFR sample rate. For $M = 2$ the first null occurs at the LFR Nyquist; providing better antialiasing effects, but introducing significant attenuation in the LFR passband. The RFS CIC will typically operate with $M = 1$.

For the LFR receiver with $M = 1$, frequencies just below the Nyquist of 2.4 MHz will have relatively poor antialiasing performance. However, these frequencies are not included in the telemetered LFR spectra, which only includes frequencies up to 1.7 MHz. In the frequency range from 1.3 to 1.7 MHz, the telemetered LFR and HFR data will overlap, and the selected LFR and HFR frequencies have been chosen to match in order to allow accurate intercalibration. In this overlap range, it will be possible to identify any aliased signals (aliased down from 3.1 to 3.5 MHz) in the LFR by comparing to the HFR spectrum. Below 1.3 MHz, where there will be no overlap between LFR and HFR, the CIC algorithm should be sufficient to remove aliased signals (aliased down from 3.5 MHz and above), as shown in Figure 7a. Should it be determined on orbit that further antialiasing is required, the $M = 2$ mode can be commanded via flight software.

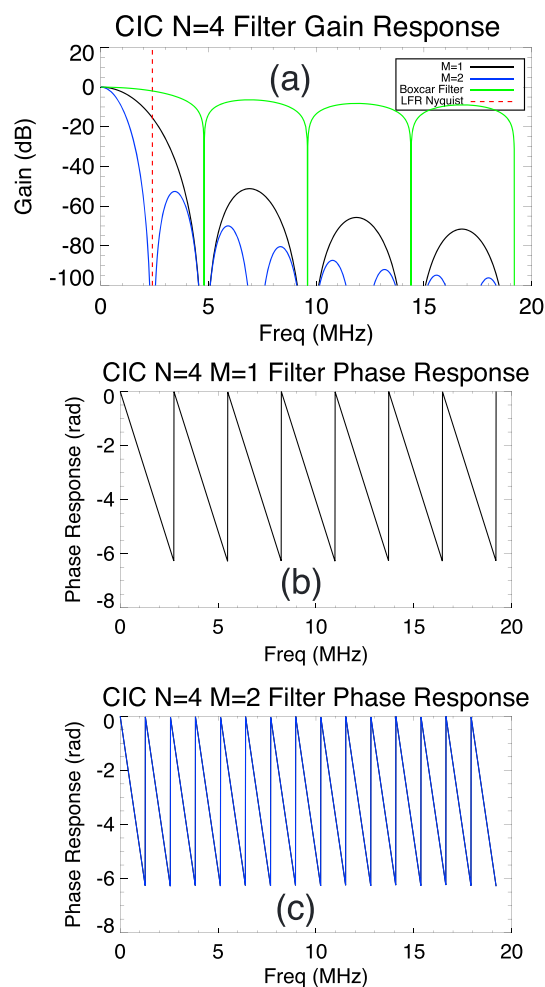


Figure 7. CIC filter response for the LFR mode of RFS. The CIC filter provides rejection of aliased signals in the LFR frequency range. (a) The gain response of the CIC filter. (b and c) The phase response for the $M = 1$ and $M = 2$ modes of the CIC filter.

The CIC phase response is linear in frequency, as shown in Figures 7b and 7c for the $M = 1$ and $M = 2$ modes. For onboard cross correlations, the same value of M will always be set for the two LFR input channels, so there will be no relative phase difference generated by the CIC.

5. RFS Operations

5.1. Operating Modes

In normal operation, the RFS produces LFR and HFR autospectra and cross spectra on a regular cadence. The cadence is commandable but limited by the available telemetry for the SPP/FIELDS suite, and will typically be on the order of 8 s on orbit for the duration of the encounter phase (approximately 12 days). The default operating configuration will be two channel measurements, with one channel measuring the opposing dipole pair V1–V2, and the other channel measuring V3–V4. In this default configuration, the RFS will alternate between LFR and HFR modes.

For both LFR and HFR data, the final telemetered data product is an averaged spectrum, where the number of individual spectra in the average is ~ 80 . Averaging together individual spectra reduces the statistical noise in the telemetered spectra, at the expense of additional processing time and required memory. The number 80 is determined by the amount of averaging necessary to yield statistical noise in the spectra of ~ 0.3 dB, comparable to the performance of previous instruments [e.g., Bougeret *et al.*, 1995]. This number can be changed on orbit via flight software command.

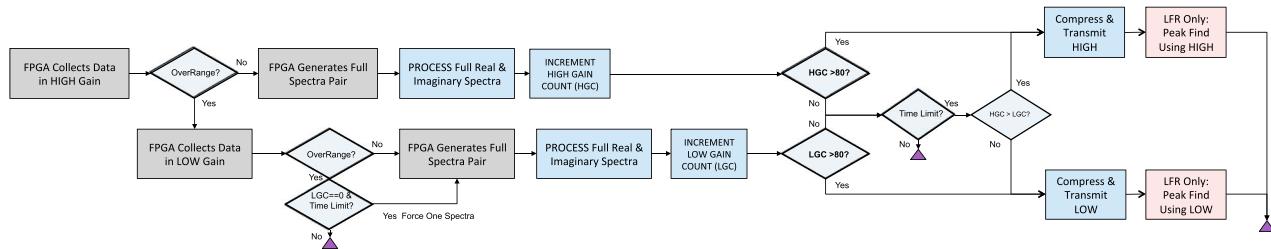


Figure 8. Flowchart of an RFS measurement interval.

During a single RFS measurement interval (for LFR or HFR), the instrument attempts to accumulate the desired number of individual spectra. The RFS always attempts to start by collecting a waveform in high-gain mode. If the signal can be measured in high gain (i.e., there are no overranges in the waveform captured by the ADC), then the FPGA creates a spectrum with the PFB/FFT and increments the count of high-gain spectra. If the signal amplitude is too high, the RFS collects a low-gain waveform and checks for overranges. If there are none, the RFS creates a spectrum and increments the count of low-gain spectra. The process restarts, accumulating spectra until either ~ 80 high-gain or low-gain spectra have been accumulated, or a time limit is reached. If more high-gain spectra have been accumulated during the interval, the high-gain spectra are averaged, compressed, and telemetered. If more low-gain spectra have been accumulated, they are used instead.

The total accumulation time is approximately 2 s in the best case scenario (no overranges in the high-gain spectra). Frequent overranges can extend the time interval required to accumulate sufficient spectra, up to the commandable preset time limit, which will typically be on the order of 4 s. If all spectra in an interval are overranged, which may occur during, e.g., an especially intense period of dust impacts, a single spectrum (which is likely to be strongly distorted by the effects of overranges) will be computed and returned.

The actual time during which measurements are made, not counting the time for the FPGA and flight software to process the spectra, is 0.85 ms for each HFR waveform (6.8 ms for LFR), multiplied by the number of spectra in the HFR or LFR measurement cycle. In a nominal case of 80 accumulated spectra over an ~ 8 s cadence, this results in an overall duty cycle of approximately 0.85% for HFR and 6.8% for LFR.

A flow chart of the RFS operation for a single LFR or HFR measurement, illustrating the accumulation of high- and low-gain spectra and the processing steps involved, is shown in Figure 8.

The RFS will detect and track the f_p plasma line in the LFR spectra. The tracker will attempt to locate f_p using a peak detection algorithm, with a backup estimator of f_p based on a model of solar wind density [Leblanc *et al.*, 1998] for time periods when the plasma peak is small and difficult to detect. As an alternative means of estimating f_p , the RFS may be able to use (raw and uncalibrated) SWEAP [Kasper *et al.*, 2015] data which will be available on board. Once the peak is detected (or estimated), a high-frequency resolution segment of the full LFR spectrum will be selected for downlink. This plasma tracking section will increase the frequency resolution $\Delta f/f$ to $\sim 1\%$, compared to the typical $\sim 4.5\%$ of the normal reduced LFR spectrum. The additional frequency resolution will enable improved ground-based analysis of QTN electron parameters. The algorithm for finding the peak is based on a similar algorithm developed for the SORBET receiver on the BepiColombo spacecraft [Moncuquet *et al.*, 2006].

Additional operating modes exist which enable the RFS to focus on specific topics of scientific interest. The HFR and LFR telemetered autospectra, which are the product of many individual HFR- and LFR-measured spectra, can optionally include a spectra of maximum amplitude in addition to the default averaged spectra. The maximum spectrum can provide a rough estimator of the variance of spectral fluctuations. The time cadence of the telemetered spectra can be increased for certain short time periods (tens of minutes per orbit) in order to study rapidly varying Type III radio burst storms, which could be possible signatures of coronal heating by small flares [Hudson, 1991; Mercier and Trotter, 1997; Saint-Hilaire *et al.*, 2013]. For extremely limited time intervals (typically less than 1 s per ~ 12 days), raw 38.4 MHz waveforms can also be telemetered for diagnostic purposes. Radio direction-finding mode, described in the following section, enables tracking of radio sources throughout the heliosphere.

During commissioning, the RFS will be turned on and will record data during the deployment of the SPP magnetometer boom and the deployment of the V1–V4 antennas. Commissioning, which will take place shortly

after launch while the spacecraft is at a distance of slightly less than 1 AU, is a critical time interval for the RFS. By comparing the spectrum measured by the antenna predeployment and during the quietest postdeployment time interval, it is possible to calibrate the antennas against the galactic synchrotron spectrum, even when the background noise of the system is of comparable magnitude to the galactic signal [Zaslavsky *et al.*, 2011]. Commissioning is the best time to observe the galaxy, since during the encounter phase the synchrotron spectrum will likely be overwhelmed by the QTN spectrum (see Figure 3).

5.2. Direction Finding

Radio direction finding is a technique that determines the direction of a radio source, using measured antenna response. Several methods have been developed which depend on how the radio emission is received and recorded. Spinning spacecraft can sometimes use demodulation techniques to determine the source direction [Fainberg *et al.*, 1972]. For three-axis-stabilized spacecraft, methods are based on autocorrelation and cross-correlation analyses between two or more antenna voltages to infer the wave electric field. These methods have been employed on STEREO [Kaiser *et al.*, 2008; Bougeret *et al.*, 2008] and Cassini [Gurnett *et al.*, 2004; Cecconi *et al.*, 2008], and will be applied for SPP. Finding the direction to a radio source is equivalent to finding the wave vector direction of the measured wave field, which is intrinsically linked to the polarization state. This information is contained in the wave field spectral matrix $S_{ij} \propto E_i E_j$, which is related to the measured antenna voltage correlations $\langle V_i V_j^* \rangle = h_i S_{ij} h_j^*$, where h_i are the components of the effective electrical antenna vector. Finding the direction to the source therefore is an inversion problem: find S_{ij} given the measured $\langle V_i V_j^* \rangle$. This can be accomplished by iterative numerical methods [Ladreiter *et al.*, 1995; Vogl *et al.*, 2004; Reiner *et al.*, 2009] or noniterative methods [Santolik *et al.*, 2003; Cecconi and Zarka, 2005; Hess, 2010]. Analytical inversion, possible for most polarizations, gives an efficient and fast solution to the problem as shown in Cecconi and Zarka [2005] for the case of two or three electric dipole antennas. In the particular case of SPP/RFS, which has four antennas, four sets of autocorrelations and six cross correlations will be obtained. Because the RFS has only two channels, the measurement of the set of autocorrelations and cross correlations is not simultaneous, and therefore, we use the assumption that physical events measured do not change on the time scale required to perform all required measurements.

In addition to single spacecraft direction finding, multispacecraft methods [Reiner *et al.*, 2009] such as triangulation will be employed, using observations from the STEREO, Wind, and Solar Orbiter spacecraft, which are likely to be operational at the same time as SPP. Use of multispacecraft observations increases the accuracy of the radio direction determination.

6. Current Status and Performance

The RFS was designed and built at the UC Berkeley Space Sciences Laboratory. The initial stage of testing and development was performed on a breadboard RFS analog section, which was built separate from the first engineering model of the DCB. Following testing of the analog breadboard, a complete flight-like engineering model (EM) of the DCB/RFS was completed in 2015. The EM was used in 2015 and early 2016 to develop and test the digital signal processing algorithms on the DCB FPGA and in the flight software. In 2016, the flight model (FM) of the DCB/RFS was constructed and is presently (as of fall 2016) in the process of FIELDS integration and test in preparation for FIELDS delivery in early 2017. The FM is the board shown in Figure 4. Breadboard, EM, and FM preamplifiers were developed and tested at Berkeley in close collaboration with the DCB/RFS development effort.

Examples of RFS performance from the FM preamplifiers and DCB/RFS are shown in Figures 9 and 10. The units of the vertical axis for each plot are the power spectral density, in V^2/Hz , of the voltage observed at the input of the high-frequency preamplifier. Eighty individual raw spectra were averaged to produce the plots in both figures.

Figure 9 was taken from a single RFS channel (Channel 1) set to monopole input from the V4 preamplifier. No input signal was provided to the RFS (the preamplifier input was terminated with a $50\ \Omega$ load). The spectrum shows the noise floor of the preamplifier–DCB/RFS signal chain, along with the performance of the PFB. Figure 9 (top) shows the full 2048 frequency channel spectrum as calculated by the PFB and FFT. The receiver was operating in high-frequency mode, with a bandwidth of 19.2 MHz. The sharp peaks in the spectrum are power converter frequencies whose primary origin is the Low Noise Power Supply (LNPS) [Bale *et al.*, 2016], which generates power at the voltages required by each subsystem of the FIELDS suite. The peaks are

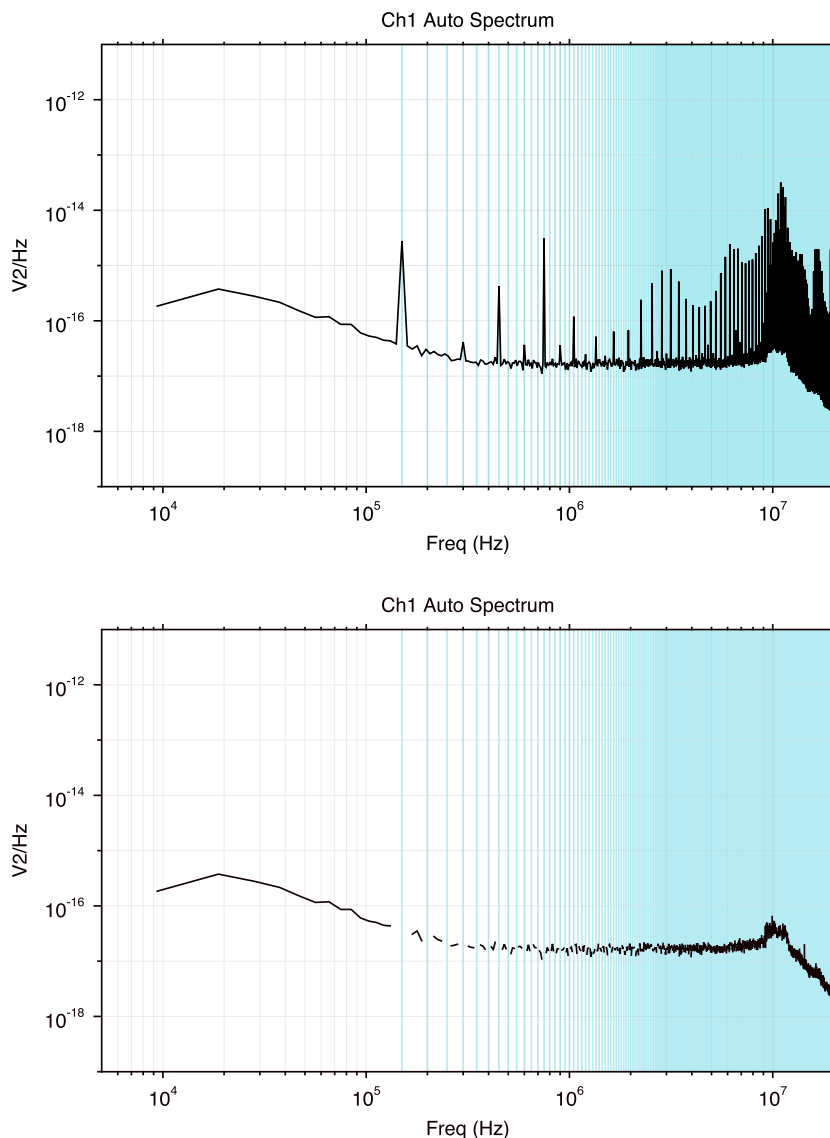


Figure 9. Example HFR spectrum with no input signal, showing the noise floor of the RFS. (top) The full spectrum and (bottom) the same data with noise peaks removed. The blue lines are located at 150 kHz + 50 × *n* kHz.

confined to the “picket fence” frequencies indicated by the pale blue lines on the plot. The power converters on the LNPS were designed to meet the same EMC specifications (described in section 4.2) that apply to all other SPP systems, so Figure 9 indicates that the RFS PFB is capable of rejecting all EMC-compliant noise sources.

The LNPS peaks extend throughout the entire bandwidth of the receiver. The PFB, discussed in section 4.2, effectively reduces the spectral leakage of the peaks, so that when the frequencies nearest the picket fence are removed, the spectrum shows no evidence of the peaks, as shown in Figure 9 (bottom). (For the figure, the peaks were removed artificially, by simply omitting the frequencies which were within $\Delta f = 9375$ Hz of a noise peak. For onboard processing, the frequencies affected by noise peaks will simply not be included in the spectral calculations, except during brief diagnostic intervals.)

Figure 10 shows the performance of the CIC filter, as discussed in section 4.3. The RFS was operating in low-frequency mode, effectively reducing the sample frequency by a factor of 8, resulting in a spectrum with a bandwidth of 2.4 MHz. Both plots in Figure 10 show the V3–V4 dipole input to RFS Channel 1. The input signal for both plots was broadband white noise into the V3 RFS preamplifier, while the V4 preamplifier has

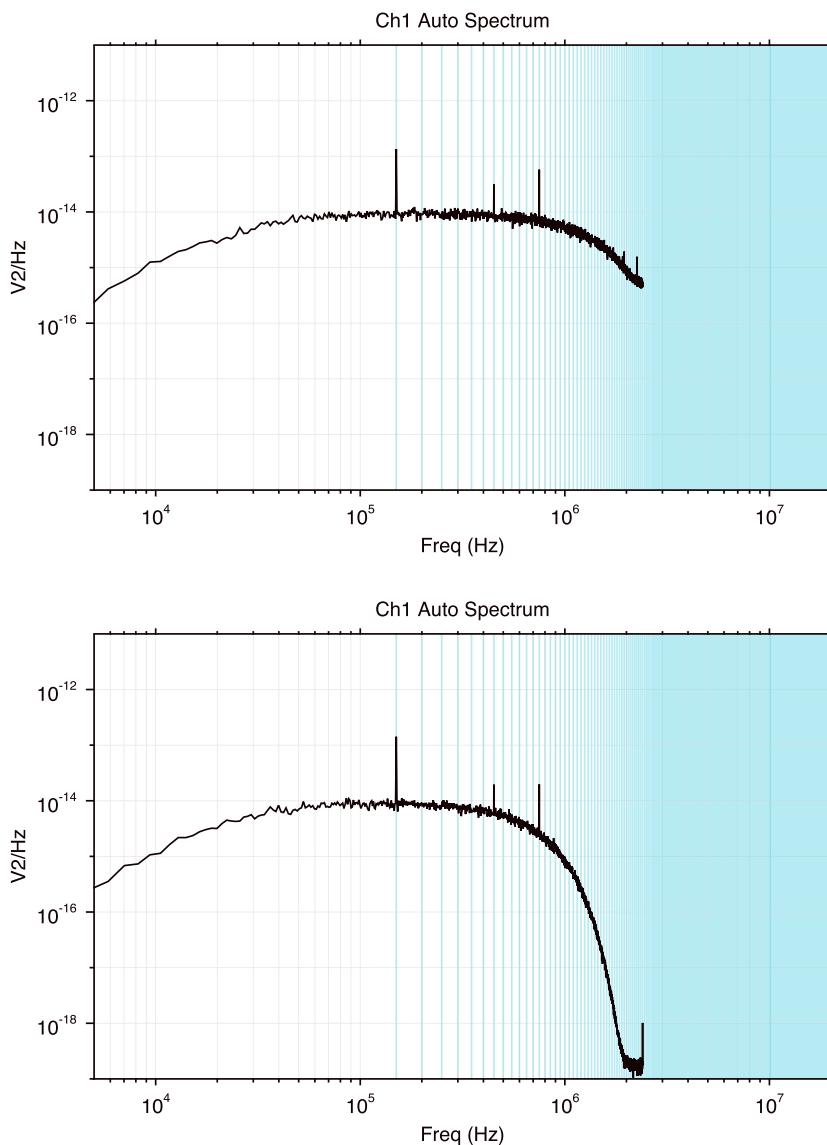


Figure 10. Example CIC performance for LFR white noise data. Shown are (top) an $M = 1$ filter and (bottom) $M = 2$.

no signal input (50Ω termination). Without filtering, both spectra would be flat above a few tens of kHz. The two plots correspond to an $M = 1$ CIC filter (Figure 10, top), with a gentle roll off above ~ 1 MHz, and an $M = 2$ CIC filter (Figure 10, bottom), with a sharp null at the Nyquist frequency of 2.4 MHz (see Figure 7).

7. Conclusion

The RFS provides the SPP/FIELDS suite with high sensitivity observations of solar radio bursts, the galactic synchrotron spectrum, and electron quasi-thermal noise at frequencies up to 19.2 MHz. The combination of the RFS analog electronics with the DCB on the same board reduces the mass and power requirements of the instrument, which are both highly constrained resources for the SPP mission. RFS digital signal processing, along with adherence to EMC specifications, enables operation of a sensitive instrument in the presence of noisy components on the SPP spacecraft. The configurable modes of the instrument allow for operational flexibility within an unexplored region of the heliosphere where operating conditions cannot be precisely known prior to launch. The RFS instrument is currently being integrated with the FIELDS suite for delivery in early 2017, and will contribute to the resolution of the science goals of FIELDS and the overall SPP mission.

Acknowledgments

The authors are grateful to the entire FIELDS team and to scientists and engineers at Berkeley and LESIA who participated in reviews and discussions. We are grateful to the two anonymous referees for comments which significantly improved this paper. Early conversations with D. Werthimer and D. MacMahon were very useful in the development of the RFS digital signal processing. We are grateful to B. Mochizuki, T. Quinn, and A. Siy for RFS integration and test support. The data presented in this paper are generated from formulas given in the text and references, or included in the supporting information. This work was supported by NASA contract NNN06AA01C.

References

- Bale, S. D., et al. (2008), The Electric Antennas for the STEREO/WAVES Experiment, *Space Sci. Rev.*, *136*, 529–547, doi:10.1007/s11214-007-9251-x.
- Bale, S. D., et al. (2016), The FIELDS instrument suite for solar probe plus—Measuring the coronal plasma and magnetic field, plasma waves and turbulence, and radio signatures of solar transients, *Space Sci. Rev.*, *204*, 49–82, doi:10.1007/s11214-016-0244-5.
- Bougeret, J.-L., et al. (1995), Waves: The radio and plasma wave investigation on the Wind spacecraft, *Space Sci. Rev.*, *71*, 231–263, doi:10.1007/BF00751331.
- Bougeret, J. L., et al. (2008), S/WAVES: The radio and plasma wave investigation on the STEREO mission, *Space Sci. Rev.*, *136*, 487–528, doi:10.1007/s11214-007-9298-8.
- Briand, C. (2009), Plasma waves above the ion cyclotron frequency in the solar wind: A review on observations, *Nonlinear Processes Geophys.*, *16*, 319–329, doi:10.5194/npg-16-319-2009.
- Cane, H. V. (1979), Spectra of the non-thermal radio radiation from the galactic polar regions, *Mon. Not. R. Astron. Soc.*, *189*, 465–478, doi:10.1093/mnras/189.3.465.
- Cecconi, B., and P. Zarka (2005), Direction finding and antenna calibration through analytical inversion of radio measurements performed using a system of two or three electric dipole antennas on a three-axis stabilized spacecraft, *Radio Sci.*, *40*, RS3003, doi:10.1029/2004RS003070.
- Cecconi, B., et al. (2008), STEREO/Waves goniopolarimetry, *Space Sci. Rev.*, *136*, 549–563, doi:10.1007/s11214-007-9255-6.
- Chennamangalam, J. (2011), *The Polyphase Filter Bank Technique*, CASPER Memo 41, The Berkeley Wireless Res. Cent., The UC Berkeley Radio Astron. Lab., and The UC Berkeley Space Sci. Lab., Berkeley, Calif.
- Couturier, P., S. Hoang, N. Meyer-Vernet, and J. L. Steinberg (1981), Quasi-thermal noise in a stable plasma at rest—Theory and observations from ISEE 3, *J. Geophys. Res.*, *86*, 11,127–11,138, doi:10.1029/JA086iA13p11127.
- Donadio, M. P. (2000). [Available at <http://dspguru.com/sites/dspguru/files/cic.pdf>]
- Dulk, G. A. (1985), Radio emission from the Sun and stars, *ARA&A*, *23*, 169–224, doi:10.1146/annurev.aa.23.090185.001125.
- Dulk, G. A. (2000), *Type III Solar Radio Bursts at Long Wavelengths*, vol. 119, 115 pp., AGU Geophys. Monogr. Ser., Washington D. C.
- Eastwood, J. P., S. D. Bale, M. Maksimovic, I. Zouganelis, K. Goetz, M. L. Kaiser, and J.-L. Bougeret (2009), Measurements of stray antenna capacitance in the STEREO/WAVES instrument: Comparison of the radio frequency voltage spectrum with models of the galactic nonthermal continuum spectrum, *Radio Sci.*, *44*, RS4012, doi:10.1029/2009RS004146.
- Ergun, R. E., D. M. Malaspina, S. D. Bale, J. P. McFadden, D. E. Larson, F. S. Mozer, N. Meyer-Vernet, M. Maksimovic, P. J. Kellogg, and J. R. Wygant (2010), Spacecraft charging and ion wake formation in the near-Sun environment, *Phys. Plasmas*, *17*(7), 072903, doi:10.1063/1.3457484.
- Fainberg, J., L. G. Evans, and R. G. Stone (1972), Radio tracking of solar energetic particles through interplanetary space, *Science*, *178*, 743–745, doi:10.1126/science.178.4062.743.
- Fox, N. J., et al. (2015), The solar probe plus mission: Humanity's first visit to our star, *Space Sci. Rev.*, *204*, 7–48, doi:10.1007/s11214-015-0211-6.
- Gary, D. E., Z. Liu, and G. M. Nita (2010), A wideband spectrometer with RFI detection, *Publ. Astron. Soc. Pac.*, *122*, 560–572, doi:10.1086/652410.
- Gopalswamy, N. (2004), Recent advances in the long-wavelength radio physics of the Sun, *Planet. Space Sci.*, *52*, 1399–1413, doi:10.1016/j.pss.2004.09.016.
- Guillemant, S., V. Génot, J.-C. Matéo-Vélez, R. Ergun, and P. Louarn (2012), Solar wind plasma interaction with solar probe plus spacecraft, *Ann. Geophys.*, *30*, 1075–1092, doi:10.5194/angeo-30-1075-2012.
- Gurnett, D. A., et al. (2004), The Cassini radio and plasma wave investigation, *Space Sci. Rev.*, *114*, 395–463, doi:10.1007/s11214-004-1434-0.
- Harris, F. J. (1978), On the use of windows for harmonic analysis with the discrete Fourier transform, *Proc. of the IEEE*, *66*(1), 51–83, doi:10.1109/PROC.1978.10837.
- Hess, S. L. G. (2010), Radio goniopolarimetry: Dealing with multiple or 1-D extended sources, *Radio Sci.*, *45*, RS3003, doi:10.1029/2009RS004208.
- Hess, S. L. G., D. M. Malaspina, and R. E. Ergun (2011), Size and amplitude of Langmuir waves in the solar wind, *J. Geophys. Res.*, *116*, A07104, doi:10.1029/2010JA016163.
- Hillan, D. S., I. H. Cairns, P. A. Robinson, and A. Mohamed (2010), Prediction of background levels for the Wind WAVES instrument and implications for the galactic background radiation, *J. Geophys. Res.*, *115*, A06102, doi:10.1029/2009JA014714.
- Hogenauer, E. (1981), An economical class of digital filters for decimation and interpolation, *IEEE Trans. Acoust. Speech Signal Process.*, *29*(2), 155–162, doi:10.1109/TASSP.1981.1163535.
- Hudson, H. S. (1991), Solar flares, microflares, nanoflares, and coronal heating, *Sol. Phys.*, *133*, 357–369, doi:10.1007/BF00149894.
- Issautier, K., R. M. Skoug, J. T. Gosling, S. P. Gary, and D. J. McComas (2001), Solar wind plasma parameters on Ulysses: Detailed comparison between the URAP and SWOOPS experiments, *J. Geophys. Res.*, *106*, 15,665–15,676, doi:10.1029/2000JA000412.
- Kaiser, M. L., T. A. Kucera, J. M. Davila, O. C. St. Cyr, M. Guhathakurta, and E. Christian (2008), The STEREO mission: An introduction, *Space Sci. Rev.*, *136*, 5–16, doi:10.1007/s11214-007-9277-0.
- Kasper, J. C., et al. (2015), Solar Wind Electrons Alphas and Protons (SWEAP) investigation: Design of the solar wind and coronal plasma instrument suite for solar probe plus, *Space Sci. Rev.*, *204*, 131–186, doi:10.1007/s11214-015-0206-3.
- Kellogg, P. J. (2003), Langmuir waves associated with collisionless shocks: A review, *Planet. Space Sci.*, *51*, 681–691, doi:10.1016/j.pss.2003.05.001.
- Krupar, V., M. Maksimovic, O. Santolik, E. P. Kontar, B. Cecconi, S. Hoang, O. Kruparova, J. Soucek, H. Reid, and A. Zaslavsky (2014), Statistical survey of type III radio bursts at long wavelengths observed by the Solar TERrestrial RELations Observatory (STEREO)/Waves instruments: Radio flux density variations with frequency, *Sol. Phys.*, *289*, 3121–3135, doi:10.1007/s11207-014-0522-x.
- Ladreiter, H. P., P. Zarka, A. Lecacheux, W. Macher, H. O. Rucker, R. Manning, D. A. Gurnett, and W. S. Kurth (1995), Analysis of electromagnetic wave direction finding performed by spaceborne antennas using singular-value decomposition techniques, *Radio Sci.*, *30*, 1699–1712, doi:10.1029/95RS02479.
- Leblanc, Y., G. A. Dulk, and J.-L. Bougeret (1998), Tracing the electron density from the corona to 1au, *Sol. Phys.*, *183*, 165–180, doi:10.1023/A:1005049730506.
- Lyons, R. P. (2004), *Understanding Digital Signal Processing*, Prentice Hall PTR, N. J.
- Malaspina, D. M., L. E. O'Brien, F. Thayer, Z. Sternovsky, and A. Collette (2015), Revisiting STEREO interplanetary and interstellar dust flux and mass estimates, *J. Geophys. Res. Space Physics*, *120*, 6085–6100, doi:10.1002/2015JA021352.
- Malaspina, D. M., et al. (2016), The Digital Fields Board for the FIELDS instrument suite on the Solar Probe Plus mission: Analog and digital signal processing, *J. Geophys. Res. Space Physics*, *121*, 5088–5096, doi:10.1002/2016JA022344.

- Manning, R., and G. A. Dulk (2001), The Galactic background radiation from 0.2 to 13.8 MHz, *Astron. Astrophys.*, *372*, 663–666, doi:10.1051/0004-6361:20010516.
- Martinović, M. M., A. Zaslavsky, M. Maksimović, N. Meyer-Vernet, S. Šegan, I. Zouganelis, C. Salem, M. Pulupa, and S. D. Bale (2016), Quasi-thermal noise measurements on STEREO: Kinetic temperature deduction using electron shot noise model, *J. Geophys. Res. Space Physics*, *121*, 129–139, doi:10.1002/2015JA021710.
- Mercier, C., and G. Trotter (1997), Coronal radio bursts: A signature of nanoflares?, *Astrophys. J.*, *474*, L65–L68, doi:10.1086/310422.
- Meyer-Vernet, N., and C. Perche (1989), Tool kit for antennae and thermal noise near the plasma frequency, *J. Geophys. Res.*, *94*, 2405–2415, doi:10.1029/JA094iA03p02405.
- Meyer-Vernet, N., M. Maksimovic, A. Czechowski, I. Mann, I. Zouganelis, K. Goetz, M. L. Kaiser, O. C. St. Cyr, J.-L. Bougeret, and S. D. Bale (2009), Dust detection by the Wave Instrument on STEREO: Nanoparticles Picked up by the solar wind?, *Sol. Phys.*, *256*, 463–474, doi:10.1007/s11207-009-9349-2.
- Moncuquet, M., A. Lecacheux, N. Meyer-Vernet, B. Cecconi, and W. S. Kurth (2005), Quasi thermal noise spectroscopy in the inner magnetosphere of Saturn with Cassini/RPWS: Electron temperatures and density, *Geophys. Res. Lett.*, *32*, L20S02, doi:10.1029/2005GL022508.
- Moncuquet, M., H. Matsumoto, J.-L. Bougeret, L. G. Blomberg, K. Issautier, Y. Kasaba, H. Kojima, M. Maksimovic, N. Meyer-Vernet, and P. Zarka (2006), The radio waves and thermal electrostatic noise spectroscopy (SORBET) experiment on BEPICOLOMBO/MMO/PWI: Scientific objectives and performance, *Adv. Space Res.*, *38*, 680–685, doi:10.1016/j.asr.2006.01.020.
- Novaco, J. C., and L. W. Brown (1978), Nonthermal galactic emission below 10 megahertz, *Astrophys. J.*, *221*, 114–123, doi:10.1086/156009.
- Oswald, T. H., W. Macher, H. O. Rucker, G. Fischer, U. Taubenschuss, J. L. Bougeret, A. Lecacheux, M. L. Kaiser, and K. Goetz (2009), Various methods of calibration of the STEREO/WAVES antennas, *Adv. Space Res.*, *43*, 355–364, doi:10.1016/j.asr.2008.07.017.
- Press, W. H., S. A. Teukolsky, W. T. Vetterling, and B. P. Flannery (1992), *Numerical recipes in FORTRAN. The art of scientific computing*, 2nd ed., Cambridge Univ. Press, New York.
- Proakis, J. G., and D. G. Manolakis (2007), *Digital Signal Processing*, Pearson Prentice Hall, Englewood Cliffs.
- Reid, H. A. S., and H. Ratcliffe (2014), A review of solar type III radio bursts, *Res. Astron. Astrophys.*, *14*, 773–804, doi:10.1088/1674-4527/14/7/003.
- Reiner, M. J., and R. J. MacDowall (2015), Electron exciter speeds associated with interplanetary type III solar radio bursts, *Sol. Phys.*, *290*, 2975–3004, doi:10.1007/s11207-015-0779-8.
- Reiner, M. J., K. Goetz, J. Fainberg, M. L. Kaiser, M. Maksimovic, B. Cecconi, S. Hoang, S. D. Bale, and J.-L. Bougeret (2009), Multipoint observations of solar type III radio bursts from STEREO and wind, *Sol. Phys.*, *259*, 255–276, doi:10.1007/s11207-009-9404-z.
- Rucker, H. O., W. Macher, R. Manning, and H. P. Ladreiter (1996), Cassini model rheometry, *Radio Sci.*, *31*, 1299–1312, doi:10.1029/96RS01972.
- Saint-Hilaire, P., N. Vilmer, and A. Kerdraon (2013), A decade of solar type III radio bursts observed by the Nançay radioheliograph 1998–2008, *Astrophys. J.*, *762*(1), 60, doi:10.1088/0004-637X/762/1/60.
- Salem, C., J.-M. Bosqued, D. E. Larson, A. Mangeney, M. Maksimovic, C. Perche, R. P. Lin, and J.-L. Bougeret (2001), Determination of accurate solar wind electron parameters using particle detectors and radio wave receivers, *J. Geophys. Res.*, *106*, 21,701–21,717, doi:10.1029/2001JA900031.
- Santolik, O., M. Parrot, and F. Lefeuvre (2003), Singular value decomposition methods for wave propagation analysis, *Radio Sci.*, *38*, 1010, doi:10.1029/2000RS002523.
- Steinberg, J. L., S. Hoang, and G. A. Dulk (1985), Evidence of scattering effects on the sizes of interplanetary Type III radio bursts, *Astron. Astrophys.*, *150*, 205–216.
- Stone, R. G., J. L. Bougeret, J. Caldwell, P. Canu, Y. de Conchy, N. Cornilleau-Wehrin, M. D. Desch, J. Fainberg, K. Goetz, and M. L. Goldstein (1992), The unified radio and plasma wave investigation, *Astron. Astrophys.*, *92*, 291–316.
- United States Department of Defense (MIL) (1999), MIL-STD-461E: Requirements for the control of electromagnetic interference characteristics of subsystems and equipment, in *Department of Defense Interface Standard*, vol. E, pp. 91–101, U.S. Dep. of Defense.
- Vogl, D. F., et al. (2004), In-flight calibration of the Cassini-Radio and Plasma Wave Science (RPWS) antenna system for direction-finding and polarization measurements, *J. Geophys. Res.*, *109*, A09S17, doi:10.1029/2003JA010261.
- Weber, R. R. (1978), Low frequency spectra of type III solar radio bursts, *Sol. Phys.*, *59*, 377–385, doi:10.1007/BF00951843.
- Zaslavsky, A., N. Meyer-Vernet, S. Hoang, M. Maksimovic, and S. D. Bale (2011), On the antenna calibration of space radio instruments using the galactic background: General formulas and application to STEREO/WAVES, *Radio Sci.*, *46*, RS2008, doi:10.1029/2010RS004464.
- Zaslavsky, A., et al. (2012), Interplanetary dust detection by radio antennas: Mass calibration and fluxes measured by STEREO/WAVES, *J. Geophys. Res.*, *117*, A05102, doi:10.1029/2011JA017480.
- Zouganelis, I., M. Maksimovic, N. Meyer-Vernet, S. D. Bale, J. P. Eastwood, A. Zaslavsky, M. Dekkali, K. Goetz, and M. L. Kaiser (2010), Measurements of stray antenna capacitance in the STEREO/WAVES instrument: Comparison of the measured voltage spectrum with an antenna electron shot noise model, *Radio Sci.*, *45*, RS1005, doi:10.1029/2009RS004194.